PCCP

ROYAL SOCIETY OF CHEMISTRY

PAPER

View Article Online
View Journal | View Issue

Cite this: *Phys. Chem. Chem. Phys.*, 2024, **26**, 22442

Neutral pH Fenton and photo-Fenton activity of Mo-doped iron-pyrite particles†

Maheswari Yadav,[a] Uttam Kumar,[a] Arup Kumar De[ab] and Indrajit Sinha *[a]

Low H_2O_2 utilization efficiency for hydroxyl radical generation, acidic pH, and recyclability are critical limitations of heterogeneous Fenton and photo-Fenton catalysts. The present research shows that the optimum Mo doping of FeS_2 particles can largely alleviate these catalysis constraints. A solvothermal protocol was followed to prepare polyvinyl pyrrolidone (PVP) stabilized FeS_2 and Mo-doped FeS_2 particles. XRD observations showed that Mo doping increases the lattice parameters of FeS_2. The band gap of the Mo-doped FeS_2 particles decreased to 1.58 eV from the 2.24 eV value exhibited by pure FeS_2 particles. Structural and electronic structure DFT calculations support these results. The Fenton and photo-Fenton *p*-nitrophenol (PNP) degradation at neutral pH on PVP-stabilized Mo-doped FeS_2 and FeS_2 particles were examined. The photo-Fenton results were substantially better than under Fenton conditions. The best PNP degradation photo-Fenton turnover frequency (TOF) recorded was 254.50 μmol g^{-1} min^{-1} on the PVP stabilized 4% Mo-doped FeS_2 sample. The Mo-doped FeS_2 catalysts were stable under photo-Fenton recycling, and the H_2O_2 (1.66 mM) required for these reactions was significantly lower than most reports (30–6000 mM). Given the economic importance of the latter in Fenton/photo-Fenton reactions, H_2O_2 normalized turnover frequency (13.85 and 153.31 mg^{-1} min^{-1} L for Fenton and photo-Fenton) values were used to evaluate catalytic activities.

Received 23rd February 2024,
Accepted 3rd August 2024

DOI: 10.1039/d4cp00793j

rsc.li/pccp

1. Introduction

The Fenton reaction is a well-known method for degrading organic pollutants in wastewater from various sources. The conventional homogeneous Fenton reaction involves the reductive cleavage of H_2O_2 to generate hydroxyl radicals using a ferrous salt as a catalyst ($Fe^{2+} + H_2O_2 \rightarrow Fe^{3+} + OH^- + {}^{\bullet}OH$). The hydroxyl radical released in this process is a powerful non-selective oxidant for organic molecules. The classical Fenton reaction has several limitations. While the forward reaction (Fe^{2+} to Fe^{3+} oxidation) is fast, the reverse process for the regeneration of the Fe^{2+} ions is much slower, resulting in the accumulation of Fe^{3+} salt and poor recyclability. Moreover, low pH conditions are necessary because neutral or higher pH can cause $Fe(OH)_3$ precipitation, which takes out Fe species from the catalyst. This process drastically reduces the recyclability of Fe^{2+} species to Fe^{3+} and back. Lower pH prevents this phenomenon and ensures better catalyst utilization and consequently hydroxyl radical production. Another critical issue is the H_2O_2 utilization efficiency, which determines the running cost of commercial Fenton and photo-Fenton processes. Most advanced oxidation processes report H_2O_2 concentration in the 30–6000 mmol L^{-1} range.[1] Only a few homogeneous or heterogeneous Fenton/photo-Fenton publications give the H_2O_2 utilization data.

Most heterogeneous Fenton catalysts (particles or nanoparticles) also exhibit improved Fenton activity under acidic conditions. The conversion of Fe^{3+} to Fe^{2+} ($Fe^{3+} + {}^{\bullet}OOH \rightarrow Fe^{2+} + H^+ + O_2$) for the catalyst regeneration is still the main rate-limiting step. Only a few heterogeneous catalysts have been investigated for their neutral pH Fenton activities. Thus, developing effective nanocatalysts that can operate a Fenton-like reaction under neutral pH conditions is a topical area of research. Extensively chelated Fenton nanocatalysts (succinates, citrates, tartrates, ethylene diamine tetra-acetic acid, *etc.*) remain soluble even under neutral pH conditions[2–5] and prevent the precipitation of $Fe(OH)_3$. Nonetheless, these chelating agents also scavenge hydroxyl radicals which slows down the degradation kinetics of the target organic pollutants.

Recently, Zhou *et al.* demonstrated that glutathione-functionalized magnetite nanoparticles catalyzed Fenton-like degradation of dichlorophenol under neutral pH conditions.[6] Apparently, the thiol group in the glutathione molecule is responsible for its Fenton catalytic activity.[7] In this context, there are a few reports in recent literature on the use of iron

[a] *Department of Chemistry, Indian Institute of Technology (Banaras Hindu University), Varanasi 221005, India*
[b] *Knowledge Resources & Information Technology Division, CSIR-National Metallurgical Laboratory, Jamshedpur-831007, India.*
E-mail: isinha.apc@iitbhu.ac.in

† Electronic supplementary information (ESI) available. See DOI: https://doi.org/10.1039/d4cp00793j

pyrite nanoparticles as heterogeneous Fenton catalysts at neutral pH. For instance, Bae *et al.*[8] reported diclofenac degradation under near-neutral Fenton conditions on FeS_2 particles. There is also a report on the Fenton catalytic activity for *p*-nitrophenol (PNP) degradation on natural and synthesized iron pyrite particles.[9] Nevertheless, these publications have either not investigated the recyclability of FeS_2 particles as Fenton catalysts for PNP degradation or the ref. 8 recyclability of bare FeS_2 particles after the first cycle (of PNP degradation) is quite poor. The poor recyclability is mainly because the reconversion of Fe^{3+} to Fe^{2+} requires catalyst degradation by sulfate formation.

Though FeS_2 is a small bandgap semiconductor, there are very few investigations on the photo-Fenton properties of these materials.[8] The recyclability reported by Zeng *et al.* for photo-Fenton PNP degradation on bare FeS_2 is worse than the Fenton case. Molybdenum, like Fe, also exists in multiple oxidation states, which can help regenerate Fe^{2+} from Fe^{3+} sites. Furthermore, such doping can also slow down photoexcited charge recombination kinetics,[10] enhancing the photo-Fenton activity of the catalyst. It has been reported that MoS_2 is a good co-catalyst for the homogeneous Fenton reaction reduction of H_2O_2.[11] Given the above literature survey, the research in the present article investigates the Fenton and photo-Fenton PNP degradation activities of molybdenum-doped and undoped PVP (polyvinyl pyrrolidone) stabilized FeS_2 particles. PNP is a non-degradable toxic intermediate synthesizing various chemicals in the pharmaceutical and dyes industries. It can cause several health issues like drowsiness, headaches, nausea, *etc.* PNP oxidative degradation is critical to water purification.

There is no investigation on the effect of Mo-doping of FeS_2 on its Fenton and photo-Fenton PNP degradation activity. Hence, the present research investigates Fenton and photo-Fenton activities of Mo-doped FeS_2 particles for PNP degradation under neutral pH conditions. Mo exists in +4 and +6 oxidation states. It is possible that electron transfer from the dopant (in its +4 state) to Fe^{3+} can reduce it back to Fe^{2+} state. The latter should enhance the Fenton/photo-Fenton activity of the catalyst. Consequently, the investigations in the present research emphasize the catalyst utilization, H_2O_2 requirement, and recyclability of the catalyst under Fenton and photo-Fenton conditions. A solvothermal protocol was used to prepare polyvinyl pyrrolidone (PVP) stabilized Mo-doped FeS_2 particles with 1, 4, and 8-mole percent Mo dopants. PVP functionalization of the particle surface reduced the interaction of the sulfur on the surface with the aqueous medium. The prepared materials were thoroughly characterized by X-ray diffraction (XRD), transmission electron microscopy (TEM), X-ray photoelectron spectroscopy, *etc.* Photoluminescence and solid-state UV visible spectroscopy were used to analyze the excited species recombination and the optical band gap of the prepared materials. Plane-wave density functional theory (DFT) calculations were carried out along with exhaustive experimental investigations. The DFT results complement experimental observations on the dopant (Mo) position in the FeS_2 lattice. Furthermore, the change in the electronic structure of FeS_2 due to Mo doping was also calculated. The DFT calculation inputs help ascertain possible Fenton and photo-Fenton mechanisms.

2. Experimental section

2.1 Experimental reagents

$FeCl_2{\cdot}4H_2O$ and elemental sulfur were purchased from SRL Chemical. $(NH_4)_6Mo_7O_{24}{\cdot}4H_2O$, the molybdenum precursor, was purchased from Sigma Aldrich. Polyvinyl pyrrolidone (PVP), NaOH, and ethylene glycol (EG) were supplied by Merck. Isopropyl alcohol (IPA) was purchased from Himedia. PNP was procured from Spectrochem Mumbai. All chemicals were of analytical grade and used without further purification. 30% W/V H_2O_2 was purchased from Qualigens.

2.2 Iron pyrite synthesis

A solvothermal method was used to synthesize PVP-stabilized iron pyrite particles.[12,13] 0.32 g of $FeCl_2{\cdot}4H_2O$ was dissolved in 50 mL ethylene glycol with vigorous stirring. Next, 1.16 g of PVP was added and stirred to obtain a yellow-colored solution. This solution was poured into 10 mL of 1 M NaOH solution. The color of the reaction mixture changed from yellow to dark green. After half an hour of vigorous stirring, 0.33 g of elemental sulfur was added to the reaction mixture. Stirring was continued until the color of the reaction mixture changed from dark green to dark red color. Finally, the reaction mixture was transferred to a 100 mL autoclave and kept in an oven at 180 °C for 24 hours. The reaction mixture was allowed to cool at room temperature. The resultant black suspension was centrifuged, and the precipitate was washed multiple times with double distilled water. Ethanol was used for the final washing. The washed product was dried at 50 °C overnight. The powder sample was heated at 100 °C for one hour in a vacuum oven to remove excess elemental sulfur in the product. Hereafter, the abbreviation Py denotes this PVP-stabilized iron pyrite sample.

2.3 Molybdenum doped iron pyrite synthesis

The weights of $(NH_4)_6Mo_7O_{24}{\cdot}4H_2O$ and $FeCl_2{\cdot}4H_2O$ were taken such that the percentage of Mo in the doped FeS_2 was 1, 4, and 8 moles% only. Hereafter, the 1, 4, and 8 moles percentages of Mo-doped FeS_2 samples were denoted as Py_1, Py_4, and Py_8 respectively. Py_1, Py_4, and Py_8 were prepared using 1, 4, and 8 moles percentage $(NH_4)_6Mo_7O_{24}{\cdot}4H_2O$ of $FeCl_2{\cdot}4H_2O$. Doped FeS_2 samples were prepared by dissolving Mo and Fe precursors (in the desired ratio) in 50 mL ethylene glycol with continuous stirring in the first step of the earlier discussed Py preparation protocol. The rest of the steps were the same as in the Py preparation protocol.

2.4 Fenton reaction catalysis protocol

2 mg of catalyst powder was added into the 2 mL double distilled water. Further, this mixture was sonicated for 1 hour using a bath sonicator. In each experiment, 50 μL of 2 mg/2 mL catalyst suspension was added to 3 mL of 10 ppm aqueous solution of the target organic pollutant (PNP) in a 4 mL cuvette. The prepared mixture was stored in the dark for 90 minutes with continuous stirring to establish adsorption–desorption equilibrium. The Fenton reaction was started by adding appropriate amounts of H_2O_2 to this reaction mixture. Fenton activity

of the catalyst was evaluated for the degradation of PNP in an aqueous solution. The change in the UV-visible spectrum of the target organic molecule with time at room temperature was used to monitor the degradation kinetics. The hydroxyl radical is expected to be the active species in a Fenton oxidation reaction. To confirm this a Fenton catalysis experiment was carried out in the presence of isopropyl alcohol (IPA), a hydroxyl radical scavenger.

2.5 Photo-Fenton experiment details

The photo-Fenton activities of the synthesized catalysts were examined for PNP degradation under cool white LED visible light irradiation. In each experiment, 30 μL of 2 mg/2 mL catalyst suspension was added to 10 ppm PNP (3 mL volume) aqueous solution. The prepared mixture was stored in the dark for 60 min with continuous stirring to establish adsorption–desorption equilibrium. Now, an appropriate amount of H_2O_2 was added to this mixture. After this, the mixture was placed under a 14 W Philips cool white LED light chamber to check its photo-Fenton activity. The absorption spectra of the mixture were recorded every 2 min time interval. The photo-Fenton scavenger experiment protocol was similar to that outlined in the previous sub-section but was done under a cool white LED light source.

2.6 Recyclability experiment details

The reusability of the catalysts prepared in this study was investigated by the following protocol. At the end of a Fenton or photo-Fenton experiment, the reaction mixture was centrifuged to recover the catalyst. The recovered catalyst after each cycle was washed several times with double distilled water, dried, and weighed. The PNP degradation obtained after the first cycle was assumed to be 100%. The recovered catalyst was then used for the next cycle. The rest of the procedure for catalyst reuse was the same as the first cycle. PNP degradation obtained in subsequent cycles was calculated relative to that obtained in the first cycle. The photo-Fenton recyclability protocol was similar to the Fenton reaction except for the photocatalysis under a cool white LED light source.

2.7 Characterization

X-ray diffractions of Py, Py_1, Py_4, and Py_8 powder samples were carried out on a Rigaku Mini-X 600 (Japan) instrument using Cu Kα radiation (1.54046 Å) from 2θ value 5° to 90° at a 5° min^{-1} scan rate and 0.01 step size. The Shimadzu Pharmaspec UV-1700 model was used for the solid-state UV-visible diffuse reflectance spectroscopy (UV-DRS) in the 200–800 nm spectral range. UV-visible spectra of the targeted organic pollutants (in an aqueous medium) were monitored regularly on an Agilent Cary 60 instrument. X-ray photoelectron spectroscopy (XPS) determined the elements making the catalyst surface and their oxidation states. XPS also gave the valence band position of the prepared FeS_2 materials. Scanning electron microscopy (SEM) images were taken on Nova Nano SEM 450. The Fluoromax Plus model (Horiba) was used for the photoluminescence studies.

2.8 Computational details

All plane-wave DFT calculations were performed using the MedaA Vienna *ab initio* simulation package (VASP). The generalized gradient approximation – Perdew–Burke–Ernzerhof (GGA–PBE) functional was used to optimize the structure and calculate the defect formation energy.[14] Initially, a 2 × 2 × 2 supercell was built from the FeS_2 unit cell (Card No: COD 9013069). The supercell was optimized using a 4 × 4 × 4 *k*-point mesh size and 400 eV plane wave basis set energy cut-off.[15] The optimized FeS_2 model is labeled as P_0. Mo-doping of FeS_2 can happen either by substituting a Fe site or by the dopant atom occupying an interstitial (hole) position. Thus, two models were constructed. One has a Fe atom substituted by a Mo atom, and in the second, Mo was placed in an interstitial position. Hereafter, the substituted and interstitial Mo-doped models are denoted by P_1 and P_2 models, respectively (Fig. 1).

3. Results and discussion

3.1 Characterization

3.1.1 XRD analysis. Fig. 2(a) shows the powder XRD of iron pyrite (Py) and Mo-doped iron pyrite samples (Py_1, Py_4, and Py_8). The XRD peaks of sample Py appear at 2θ values: 28.49°, 33.02°, 37.04°, 40.74°, 47.38°, 56.32°, 59.02°, 61.64°, 64.21°, 76.49°, and 78.90°.[12] These correspond to (111), (200), (210), (211), (220), (311), (222), (023), (321), (331), and (420) planes of the standard Face center cubic unit cell (JCPDS 71-2219) phase of iron pyrite. The Mo-doped FeS_2 samples (Py_1, Py_4, and Py_8) also displayed XRD patterns having peaks observed for the Py sample. Notably, the XRD patterns of doped or undoped FeS_2 do not show peak(s) of marcasite or any other impurity (Fe_3S_4, FeS, *etc.*) phase peaks.

Fig. 2(b) compares the most intense (200) peaks for Py, Py_1, Py_4, and Py_8 samples. An increase in Mo doping till 4% doping (Py_4) shifted the (200) peak position slightly towards the smaller 2θ side, indicating lattice expansion.[16] However, the peak shifting is not the same in all doped samples. Fig. 2(c) shows the lattice parameter *versus* the dopant mole percent scatter plot. The lattice parameter increases with doping till 4% Mo. The lattice parameter of the Py_8 sample deviates only slightly from the Py sample. Note that 0.79 and 0.75 nm are the effective ionic radii of Mo^{4+} and Fe^{2+}, respectively.[17,18] Since the difference between these two ionic radii is very small (5.06%), it is possible that Mo^{4+} substitutes Fe^{2+} in the FeS_2 lattice. We come back to this issue while discussing the DFT calculation results. Furthermore, peak broadening increased until 4% Mo doping of the FeS_2 system. Py, Py_1, Py_4, and Py_8 crystallite sizes were 34.83 nm, 30.57 nm, 27.40 nm, and 29.80 nm, respectively. Thus, sample Py_4 has the least crystallite size among all samples. Table M1 (ESI†) shows the calculation, reading, and instrument precision error percentage in lattice parameter calculation. All these errors are negligible.

3.1.2 SEM analysis. The morphology and size of nanoparticles have been determined by analyzing the SEM images of the doped and undoped FeS_2 samples. Fig. M1(a–c) (ESI†)

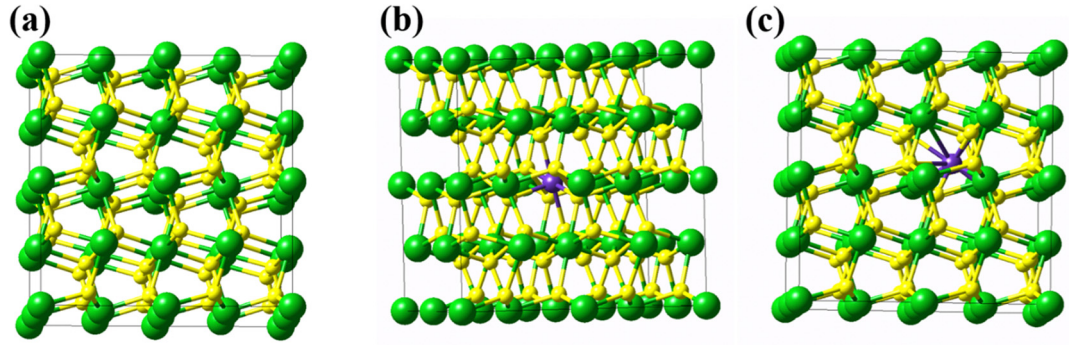

Fig. 1 (a) The iron pyrite 2 × 2 × 2 supercell, (b) Mo at the substituted position (P_1 model), and (c) Mo at the interstitial position (P_2 model). In the supercell, the green, yellow, and purple balls denote Fe atoms, S dimer, and Mo atoms respectively.

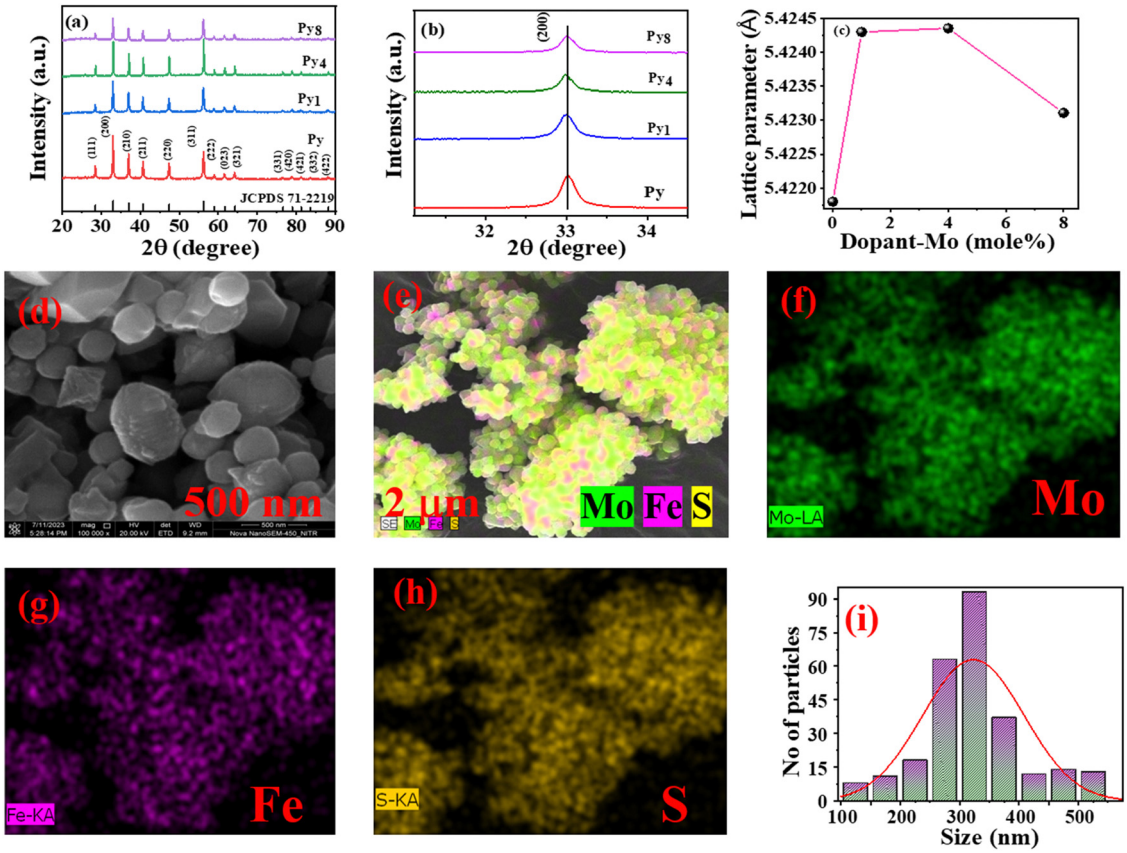

Fig. 2 (a) Powder XRD patterns of Py, Py_1, Py_4, and Py_8 samples. (b) FeS_2(200) peak position with Mo doping. (c) change in lattice parameter with Mo-doping of FeS_2. (d) SEM image of the Py_4 sample. (e) SEM image of region subjected to elemental mapping. (f) displays the elemental map of Mo. (g) Fe. (h) S atoms, and (i) particle size distribution of this sample.

shows the SEM images of Py, Py_1, and Py_8 samples. Mo doping changes the average size of the particles and their morphologies. The Py sample's particle shape resembles a square base polyhedron. Length-wise particle sizes of sample Py are larger than 2 μm (with ~600–700 nm width). The Py_1 sample consists of large 2D sheets stacked on each other. Moreover, 2 to 3 μm long (and ~100 nm wide) fiber-like anisotropic particles are on top of such aggregated sheets. In contrast to these, the Py_8 sample SEM shows stacked 100–200 nm 2D sheets.

Fig. 2(d) displays a typical SEM micrograph of the Py_4 sample. The particles are roughly spherical. Fig. 2(e) gives the SEM image of the region over which elemental mapping has been carried out. The elemental mapping of the Py_4 sample shows that Fe, S, and Mo are uniformly distributed in the particles making up the region. Fig. 2(i) gives the particle size distribution of the Py_4 sample, plotted using statistics over 270 particles. This sample's average particle size is approximately 325 nm.

3.1.3 UV-DRS analysis. The Kubelka–Munk function was used for calculating the solid-state absorbance from the reflectance of the powder sample. Fig. 3(a) shows the UV-DRS absorbance plots of the Py, Py_1, Py_4, and Py_8 samples. Fig. 3(b) shows the Tauc plots of Py, Py_1, Py_4, and Py_8 samples plotted using eqn (1).[19,20]

$$(\alpha h\vartheta)^{\frac{1}{n}} = (h\vartheta - E_g) \quad (1)$$

In eqn (1) 'h' is Planck's constant, ν is the frequency, and E_g is the band gap of the sample. The value of n is 2 and 0.5 for the indirect band gap and direct band gap, respectively.

The x-axis intercept of the fit to the linear portion of the Tauc plot gives the band gap of the sample. The direct band gap of the Py sample is 2.24 eV, in agreement with the previously reported PVP-stabilized iron pyrite nanoparticle band gap in literature.[21,22] The band gap decreased after Mo-doping to 2.22, 2.16, and 1.58 eV for Py_1, Py_4, and Py_8 samples respectively.

3.1.4 Photoluminescence spectra analysis. Photoluminescence (PL) spectra show the separation and recombination of charge carriers (electrons, holes). Lower PL intensity represents the lesser electron and hole recombination. Fig. 3(c) shows the PL spectra of the synthesized samples. The excitation wavelength used for obtaining the PL spectra was 450 nm.[23] Sample Py_8 has the highest PL intensity. PL intensities of the rest of the samples follow the order Py > Py_1 > Py_4. Thus, the PL of Py_4 demonstrates the lowest intensity among all samples and it has the slowest recombination kinetics. The latter is a prerequisite for photocatalytic efficiency. As shown in later sections, the photo-Fenton efficacy of the Py_4 is the best among the investigated Mo-doped FeS_2 samples.

3.1.5 XPS analysis. XPS was used to analyze the binding states of elements in FeS_2 and Mo-doped FeS_2 samples. Fig. M2 (ESI†) shows the XPS survey spectra of Py and Py_4 samples. The Py_4 survey spectrum displays peaks corresponding to the Fe, S, and Mo, revealing the Mo-doping of the iron pyrite lattice. Casa-XPS software was used to deconvolute the high-resolution (HR) Fe 2p, S 2p, and Mo 3d spectrums. Fig. 4(a) displays the HR-XPS spectrum of the S 2p region of Py and Py_4 samples. The S 2p spectrum was deconvoluted into peaks at 162.7 eV and 163.35 eV. These peaks correspond to S $2p_{3/2}$ and S $2p_{1/2}$ orbitals of S^{2-} respectively.[24]

The core level S 2p spectrum also shows peaks at 161.57 and 164.5 eV, implying the presence of S^- ions. Thus, S^{2-} and S^- ions exist in both samples. The deconvoluted S 2p spectra (of Py and Py_4) also display small sulfate peaks at 167.68 and 168.85 eV due to slight surface oxidation. Fig. 4(b) shows the high-resolution Fe 2p XPS spectra of Py and Py_4 samples. Two major peaks at 709.96 eV and 723.30 eV denote $2p_{3/2}$ and $2p_{1/2}$ of Fe^{2+} in the Py respectively.[25] One peak of Fe^{3+} was obtained at 713.74 eV, which represents the partial oxidation of Py due to thermal treatment during sample preparation.

Fig. 4(c) shows the Mo 3d spectra of the Py_4 sample. There are two $3d_{3/2}$ and $3d_{5/2}$ peaks at 231.8 and 227.8 eV, confirming that Mo ions are present in the +4-oxidation state.[26] Fig. 4(c) also shows one peak of S 2s at 226.04 eV.[16] The Fe 2p peaks in the Py_4 sample show a 0.6 eV shift towards higher binding energy. Thus, electron density on Fe^{2+} decreased after Mo doping because of its higher electronegativity. Fig. 4(d) shows the valence band spectra of Py and Py_4 samples. In this spectrum, the valence band positions of Py and Py_4 samples are 0.276 eV and −0.254 eV respectively. Eqn (2) was used to calculate the CB position of samples.

$$E_{CB} = E_{VB} - E_g \quad (2)$$

Here, E_{CB} is the conduction band edge position, E_{VB} is the valence band position and E_g is the band gap of the sample. The CBs of Py and Py_4 samples are located at −1.9634 and −2.414 eV respectively.

3.2 DFT studies

DFT calculations were used to investigate the position of the dopant Mo atom in the FeS_2 lattice. The formation energies of the interstitial and substituted Mo-doped FeS_2 supercell models were found to elucidate this issue. The formation energies of the substituted and interstitially doped systems are calculated using eqn (3) and (4).

$$E_f = E_{defect}(\text{sub}) - \{E_{perfect}(FeS_2) - \mu_{Fe} + \mu_{Mo}\} \quad (3)$$

$$E_f = E_{defect}(\text{Interstitial}) - \{E_{perfect}(FeS_2) + \mu_{Mo}\} \quad (4)$$

In these equations, E_f is the formation energy, $E_{perfect}(FeS_2)$ is the energy of the perfect FeS_2 supercell, $E_{defect}(\text{sub})$ is the energy of the Mo-substituted FeS_2 model, E_{defect} is the energy of

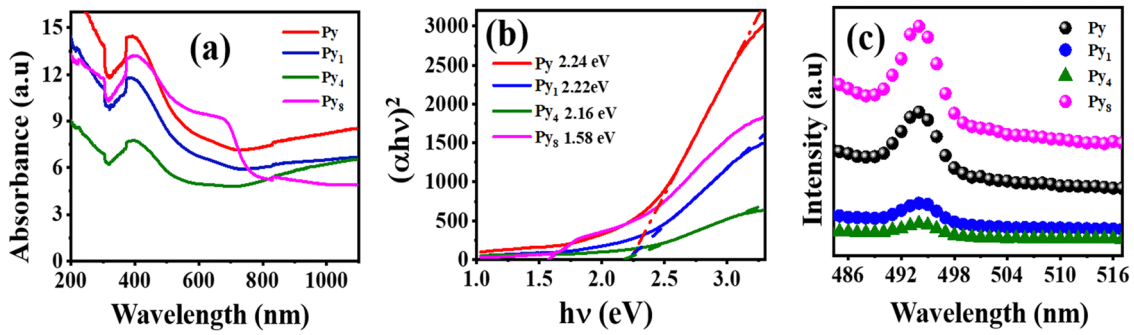

Fig. 3 (a) UV-diffusion reflectance spectra of Py, Py_1, Py_4, and Py_8 samples. (b) direct band gap plot of Py, Py_1, Py_4, and Py_8 samples. (c) Photoluminescence spectra of Py, Py_1, Py_4, and Py_8 catalyst.

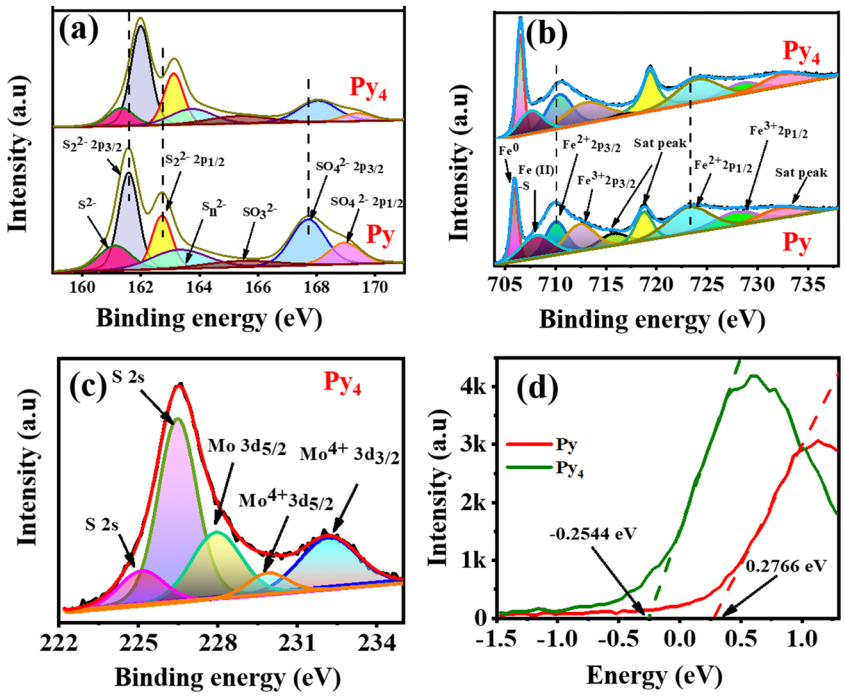

Fig. 4 (a) S 2p and (b) Fe 2p spectra of Py and Py_4 samples. (c) HR-XPS of the Mo 3d spectrum of Py_4 sample. (d) Valence band XPS spectra of Py and Py_4 samples.

the model where Mo occupies an interstitial position, μ_{Fe}, and μ_{Mo} are the chemical potentials of iron and molybdenum element.[17] The formation energies are 1.855 eV and 4.904 eV for the P_1 (substituted) and P_2 (interstitial) models. Thus, Mo-substituting a Fe in FeS_2 is more favorable than the interstitially doped model. Table 1 compares the DFT-calculated supercell parameters of the undoped and the Mo-substituted models. All dimensions of the cubic cell expand uniformly due to Mo-substituting a Fe atom in the FeS_2 model. These DFT results are exactly analogous to experimental XRD results that showed FeS_2 lattice expansion with Mo-doping till the 4% Mo level. The agreement between the DFT calculation and experimental results enables us to infer that the Mo-substitution of a Fe atom makes the FeS_2 lattice expand.

We also analyzed the electronic structures of the investigated models to better understand the photocatalytic properties of the Mo-doped FeS_2. The DOS and band structure calculations were performed on the optimized substituted doping model P_1, given its more favorable defect formation energy. The GGA–PBE functional DFT calculations severely underestimate bandgaps[27] and, in this case, we got a 0.407 eV bandgap for the P_0 model. Hence, the bandgap information obtained from DFT calculations is only qualitative. Nevertheless, the DFT calculated FeS_2 bandgap value matches the previous GGA–PBE DFT results reported in the literature.[28,29] The DFT calculations gave a much lower 0.074 eV bandgap for the Mo-substituted FeS_2 model. The decrease in bandgap after Mo-doping of the FeS_2 is qualitatively similar to the experimental results reported in Section 3.1.3. Mo 4d dopant orbital is mainly responsible for the band gap shrinking.[30,31]

Table 1 Lattice parameters of pure FeS_2 (P_0) and Mo-substituted FeS_2 (P_1) model

Dimension	Pure FeS_2	After Mo doping
X	5.395343 Å	5.412729 Å
Y	5.395343 Å	5.412729 Å
Z	5.395343 Å	5.412729 Å
A	90°	90.007825°
β	90°	90.007825°
γ	90°	90.007825°

Fig. M3 (ESI†) shows the band structures of the P_0 and P_1 models. The P_0 model displays an indirect bandgap, while P_1 has a direct bandgap. Thus, light absorption and photoexcitation increase with doping. Moreover, Mo substitution shifts the VB maximum to a higher energy (less negative value). Note that the CB position is situated at higher energy than the VB position in the standard energy scale reported by DFT calculations. However, the experimental VB and CB positions are according to the normal hydrogen electrode (NHE) scale, which is the reverse of the standard energy scale. Thus, the shift of the VB to higher energy (in the standard energy scale) corresponds to a less positive value on the NHE scale. Fig. 5(a) shows the total density of states (TDOS) of the P_0 model. The figure also displays the partial density of states (PDOS) of Fe 3d, S 3p, and S 3d orbitals. Fig. 5(c) shows the TDOS of the Mo-doped P_1 model. It also displays the PDOS of Fe 3d, S 3p, S 3d, and Mo 4d orbitals. A comparison of Fig. 5(a) and (c) shows that a Mo 4d dopant energy state appears in the bandgap region of the PDOS of the P_1 model, substantially reducing the bandgap. This qualitatively mimics the experimental results.

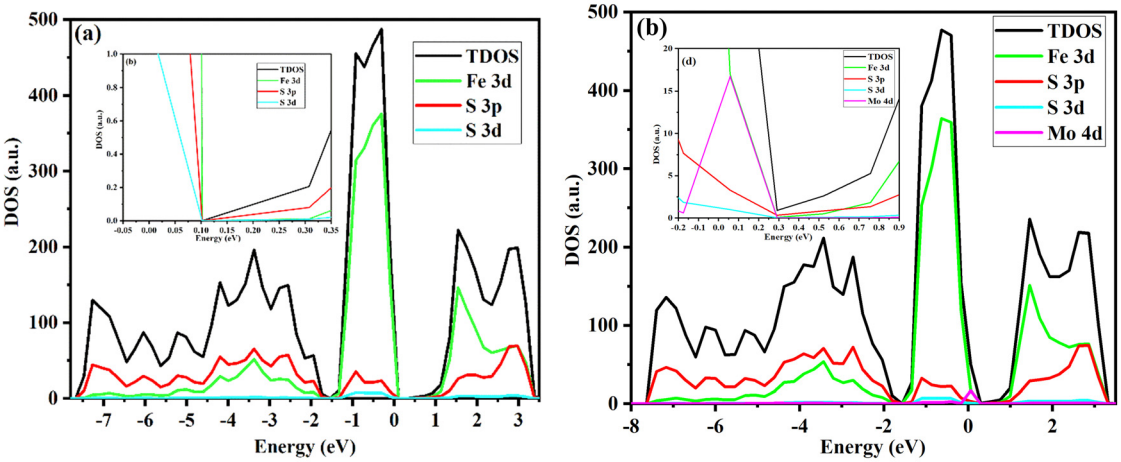

Fig. 5 TDOS and PDOS of (a) P_0 and (b) P_1 models.

3.3 Fenton catalytic activity and photo-Fenton activity

The concentration of H_2O_2 and catalyst dosage affect the Fenton reaction. An initial control experiment was performed in the dark to check the stability of PNP with H_2O_2 in the absence of a catalyst. Fig. M4(a) (ESI†) shows negligible change in the PNP concentration under these conditions. Another control experiment involved mixing 50 μL of 2 mg/2 mL Py_4 catalyst suspension with 3 mL of 10 ppm PNP aqueous solution at neutral pH. Hereafter 'neutral pH' means that the pH of the water containing the organic pollutant was neutral. The pH of the water containing the organic pollutant remained neutral even after the addition of H_2O_2. No acid was added to the water sample. However, the addition of the photo-Fenton catalyst FeS_2 changed the pH of the reaction medium. There was no addition of acid during the whole process. Please note that throughout Fenton and photo-Fenton research literature investigators imply the meaning mentioned by us when they use the term 'neutral pH'. Many publications do not report the pH of the reaction medium after the addition of the Fenton/photo-Fenton catalyst.[8,32–39] Note that the addition of the catalyst suspension reduced the pH of the PNP solution from 6.05 to 4.14 (Fig. M5(a), ESI†), in agreement with observations in previous literature.[8,40] This mixture was kept in the dark for 90 minutes with continuous stirring for adsorption–desorption equilibrium. There was a negligible change in the UV-visible absorbance spectra for PNP after 75 minutes.

The effect of different H_2O_2 dosages on the degradation of PNP was observed in the presence of 50 μL of 2 mg/2 mL Py_4 catalyst suspension. Fig. M5(b) (ESI†) shows the degradation of PNP using 12.5, 25, 50, 100, and 200 μmol of 0.5 M H_2O_2 under the earlier-mentioned conditions (Fig. M5(b), ESI†). Optimal Fenton PNP degradation was observed at 25 μmol H_2O_2. Excess H_2O_2 acted as a scavenger for hydroxy radical species.[32] Thus, 25 μmol of 0.5 M H_2O_2 (or 8.33 mmol per liter) was optimum for the oxidization of 3 mL of 10 ppm PNP solution on the Py_4 catalyst suspension. PNP degradation Fenton reaction experiments on Py, Py_1, and Py_8 samples were performed under the above-mentioned optimal reaction conditions.

The Fenton PNP degradation on different (FeS_2) catalysts follows pseudo-first-order kinetics (Fig. 6(a)). Fig. 6(a) shows the PNP degradation in the Fenton reaction *via* pseudo-first-order kinetics. PNP degradation on Py_4 was significantly faster than the other catalysts. Catalytic activity increases with Mo-doping until 4 mol% Mo. Sample Py_4 displays the best catalytic activity among the investigated materials. The catalytic activity is the least for the Py_8 particles. It is lower than observed for undoped FeS_2. Table 2 lists the investigated catalysts' turnover frequency (TOF) and first-order rate constant values. The TOF value considers the catalyst amount and can compare the efficiency of a particular reaction over different catalysts. Table 2 also gives the H_2O_2 amount that gives the optimum TOF for this Fenton reaction. Most Fenton literature reports the use of H_2O_2 substantially higher than 30 mmol per liter for optimum activity. In contrast, optimum Fenton activity, in the present investigation, was observed at a much lower 8.33 mmol per liter. For a more quantitative understanding of the effect of H_2O_2 concentration on catalytic activity, we define the concept of H_2O_2 normalized TOF value (abbreviated as HTOF). The latter is simply the TOF value divided by the H_2O_2 concentration used. Table M4 (ESI†) compares the HTOF and other parameters of the Fenton degradation of PNP over Py_4 with the HTOF activities of catalysts reported in previous literature under neutral pH conditions. One can see that Py_4 has the best neutral pH HTOF value. Note that very few publications report the TOF values of Fenton reactions. Thus, the TOF and HTOF values given in Table M4 (ESI†) have been calculated by us using relevant data available in these publications.

The first control experiment was to expose an aqueous suspension of PNP and the catalyst particles to visible light irradiation from a cool white LED source. Very little PNP degradation (<4%) occurred under this condition. Next, PNP degradation under visible light irradiation was investigated in the presence of both catalyst and H_2O_2. Fig. M6(a) (ESI†) shows the effect of PNP degradation in the presence of the different amounts of Py_4 catalyst with time. The optimum Py_4 catalyst amount was 30 μL of 2 mg/2 mL catalyst suspensions. The

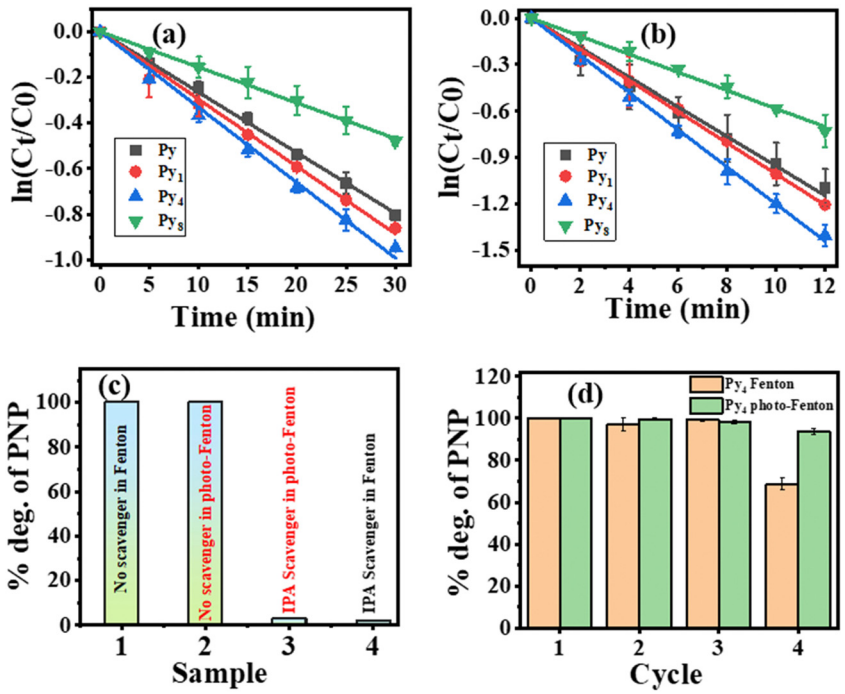

Fig. 6 (a) Pseudo-first-order reaction kinetic (with error bars) plot of PNP degradation *via* Fenton reaction in the presence of different catalysts. Reaction conditions [H_2O_2] = 25 μmol, [catalyst] = 50 μL of 2 mg/2 mL, and [PNP] = 10 mg L^{-1}. (b) pseudo-first-order reaction kinetics (with error bars) plot of PNP degradation *via* photo-Fenton reaction in the presence of different catalysts. Reaction conditions [H_2O_2] = 5 μmol, [catalyst] = 30 μL of 2 mg/2 mL, and [PNP] = 10 mg L^{-1}. (c) The effect of radical scavenger in the degradation of PNP in Fenton and photo-Fenton reaction. (d) The reusability plot of the Py_4 sample in the Fenton and photo-Fenton reaction (with error bars).

Table 2 Rate constant and TOF values for Fenton PNP degradation over undoped and doped FeS_2 samples

	Fenton reaction with [H_2O_2] = 8.33 mM			Photo-Fenton reaction with [H_2O_2] = 1.66 mM		
Sample	TOF (μmol g^{-1} min^{-1})	H_2O_2 normalized TOF (mg^{-1} min^{-1} L)	Rate constant (min^{-1})	TOF (μmol g^{-1} min^{-1})	H_2O_2 normalized TOF (mg^{-1} min^{-1} L)	Rate constant (min^{-1})
Py	97.09	11.65	0.0236	230.60	138.91	0.0954
Py_1	57.35	6.88	0.0274	243.70	146.80	0.1000
Py_4	113.16	13.85	0.0480	254.50	153.31	0.1201
Py_8	46.28	5.556	0.0144	133.34	80.32	0.0581

amount of H_2O_2 also plays a crucial role in the photo-Fenton reaction. Fig. M7(a) (ESI†) shows the effect of 2.5, 5, 10, 15, 20, and 25 μmol of 0.5 M H_2O_2 for the PNP degradation on the Py_4 catalyst. The optimum amount of 0.5 M H_2O_2 was 5 μmol. H_2O_2 amount higher than 5 μmol slowed down the PNP degradation process.

Fig. 6(b) shows the photo-Fenton degradation of PNP follows a pseudo-first-order kinetics. The third column of Table 2 displays the photo-Fenton TOF values for Py, Py_1, Py_4, and Py_8 catalysts. The rate of photo-Fenton PNP degradation increased with doping till 4% Mo in FeS_2. Thus, Py_4 displays the best photo-Fenton TOF value for PNP degradation. Sample Py_8 demonstrates a TOF value lower than observed on the Py sample. Table M5 (ESI†) compares the TOF and HTOF values of PNP degradation under photo-Fenton conditions over different catalysts reported in the literature (under neutral reaction conditions) with that of Py_4. Py_4 has the best HTOF value among the catalysts considered in this table.

Fig. 6(c) shows the percentage degradation of PNP in the presence and absence of IPA, a hydroxyl radical scavenger. Separate experiments were conducted under Fenton and photo-Fenton conditions. The Py_4 sample was used in these scavenger experiments to investigate the reactive species responsible for the Fenton and the photo-Fenton reaction. Adding IPA almost stopped PNP degradation under both Fenton and photo-Fenton conditions. Therefore, the hydroxyl ($^{\bullet}OH$) radicals are active species responsible for PNP degradation under both Fenton and photo-Fenton conditions.

Fig. 6(d) displays the recyclability of the Py_4 sample because it has the best Fenton and photo-Fenton catalytic activity for PNP degradation. Under (dark) Fenton conditions there was hardly any change in the catalytic activity of Py_4 until the end of the third cycle. However, in 4th cycle, the catalytic efficiency of Py_4 decreased to 65.88% of the TOF activity observed in the first cycle. Fig. M8 (ESI†) compares the XRDs of sample Py_4 before

use and after four cycles of reuse under (dark) Fenton conditions. After reuse, the XRD displays all FeS_2 peaks, but also has a new peak at 26.2°. The latter is attributed to the (111) plane of the Fe_7S_8 phase. The emergence of the Fe_7S_8 phase disrupts the Fenton cycle of the catalyst.

Contrary to this, the recyclability of the Py_4 catalyst under photo-Fenton conditions was significantly better. After the 4th cycle, the photo-Fenton catalytic efficiency of Py_4 samples dropped to only 95.12% of the activity observed in the 1st cycle. Thus, the photo-Fenton catalyst recyclability was appreciably better than under (dark) Fenton conditions. Table M3 (ESI†) gives complete (dark) Fenton and photo-Fenton recyclability data of sample Py_4. Fig. M8 (ESI†) compares the XRDs of the fresh Py_4 powder sample with that of the four-times recycled sample. The XRD of the reused Py_4 displays only peaks of FeS_2. Thus, the Py_4 material remains stable even after repeated use under photo-Fenton reaction conditions, explaining its high recyclability. Table M5 (ESI†) also compares the recyclability of Py_4 with previous investigations on neutral pH photo-Fenton catalysts. Please note that the MIL-100/Fe photo-Fenton catalyst (in Table M5, ESI†) uses a mercury vapor lamp as the light source without UV filter.[33] Since UV radiation can also give hydroxyl radicals from H_2O_2, therefore, the reported photo-Fenton activity may not be due to the catalyst only.

Fig. M9(a) (ESI†) shows the survey spectrum of the recycled Py_4 sample. There are some differences between the S 2p spectrum of the fresh and the recycled samples (Fig. M9(b), ESI†). Two peaks at 161.57 and 164.5 eV indicate the S^- (−1 oxidation state) species is not present in the S 2p region of the recycled XPS spectrum.[24] The area under the $2p_{3/2}$ and $2p_{1/2}$ peaks at 168.41 and 169.60 eV, due to the SO_4^{2-}, have increased by 20%, indicating increased sulfate species on the reused Py_4 sample. Fig. M9(c) (ESI†) shows peaks corresponding to $2p_{3/2}$ and $2p_{1/2}$ of Fe^{3+} at 713.74 eV and 727.5 eV, respectively.[25] The areas under these Fe^{3+} peaks have increased (10%) relative to those in the spectrum of the fresh Py_4 sample. Hence, there is an increase in the Fe^{3+} species on the reused Py_4 surface, though this is still a small percentage. Fig. M9(d) (ESI†) shows the core level Mo 3d spectrum of the Py_4 reused sample. There are two peaks at 228.44 and 230.44 eV corresponding to the $3d_{5/2}$ and $3d_{3/2}$ peaks of Mo in the +4-oxidation state.[16] The Mo 3d spectrum also shows $3d_{5/2}$ and $3d_{3/2}$ peaks at 232.67 and 235.29 eV consistent with Mo in the +6-oxidation state.[26] Thus, the recycled Py_4 sample (in contrast to the fresh Py_4 sample) shows the presence of Mo in both +4 and +6 oxidation states. The presence of Mo^{6+} on the reused Py_4 surface gives credence to the proposed reaction mechanism (see Section 3.4). The Fe and Mo leaching concentrations were determined by the ICP-MS technique. We found that the concentration of Fe and Mo elements in the tested Py_4 sample decreased by nearly 12.73% and 9.5% at the end of the 4th cycle. These percentages are relative to the elemental content of the fresh Py_4 sample. Thus, the decrease in photocatalytic efficiency to 95.12% by the fourth cycle of reuse is because of Fe and Mo leaching from the photocatalyst during the reuse of the sample.

3.4 Possible Fenton and photo-Fenton mechanism

Fenton reaction involves the oxidation of Fe^{2+} to Fe^{3+} (on the catalyst) during the reductive cleavage of H_2O_2. The latter generates hydroxyl radicals, which effectively oxidize the target organic pollutant. Effective regeneration of Fe^{2+} from Fe^{3+} on the catalyst's surface is the key to Fenton catalyst recyclability, but this step is much slower than the forward reaction. As explained earlier, the correlation between DFT calculations and XRD results shows that Mo substitutes Fe in the FeS_2 lattice. Furthermore, Mo atoms substituting Fe^{2+} in FeS_2 are in a +4-oxidation state.

The schematic in Fig. 7(a) shows the proposed Fenton catalysis mechanism. The Fenton activity is due to Fe^{2+} reducing H_2O_2. The replacement of the Fe^{2+} by Mo^{4+} results in a loss of (Fe^{2+} to Fe^{3+}) activity but also enhances the Fe^{3+} to Fe^{2+} reduction rate. The following set of reactions[34] describes this phenomenon.

$$2Fe^{3+} + Mo^{4+} \rightarrow 2Fe^{2+} + Mo^{6+} \quad (R1)$$

$$Mo^{6+} + 2e^- + 2H_2O_2 \rightarrow Mo^{4+} + 2H_2O + O_2 \quad (R2)$$

In reaction (R1), Mo^{4+} reduces Fe^{3+} to Fe^{2+}, while in the second reaction, the reduced Mo^{4+} is recovered by oxidizing H_2O_2. Hence, Mo substituting Fe decreases the forward Fenton reaction activity but enhances the regeneration of the catalyst. The two effects are opposed to each other. Thus, Py_4 demonstrates the optimal Fenton PNP degradation activity. Sample Py_8 displays lower Fenton activity because of excess Mo-doping.

As mentioned earlier, DFT calculations predict that Mo-doping would substitute a Fe atom in FeS_2, along with lattice expansion. These calculations also qualitatively showed that the Mo-doping energy state in the FeS_2 bandgap region would reduce its bandgap. Experimental results also show a bandgap reduction after Mo-doping. Besides supplying electrons for the Fe^{3+} to Fe^{2+} back reaction, the dopant Mo possibly may also influence the adsorption behaviour of the photocatalyst surface towards H_2O_2.[30,31] Additionally, XPS results show that VB and CB positions shift to lower NHE scale values. An analysis of the PDOS and TDOS of the Mo-doped FeS_2 relative to the undoped FeS_2 model shows that a Mo 4d dopant state reduces the band gap from the VB side. Furthermore, PL results show that Py_4 has slower recombination kinetics than other FeS_2 samples studied due to enhanced charge separation. In accordance with this, sample Py_4 also demonstrates the best photo-Fenton activity.

Given this background, we propose the following photo-Fenton PNP degradation mechanism. The scheme in Fig. 7(b) depicts the proposed photo-Fenton mechanism. Catalyst surface Fe^{2+} reduction of H_2O_2 generates hydroxyl radicals. Relevant IPA scavenger experiment observations show that hydroxyl radicals generated in this process oxidize PNP. Irradiating the Mo-doped FeS_2 catalyzed system with cool white LED light photoexcites the electrons from the VB to the CB of the material. The photo-excited electron reduces the Fe^{3+} to Fe^{2+}, regenerating the catalyst. The photo-excitation process converts adjacent Fe^{2+} to Fe^{3+} ions on the VB side. Mo^{4+} dopants reduce these Fe^{3+} to Fe^{2+} cations. Mo^{4+} is regenerated from Mo^{6+} by H_2O_2 oxidation on it. Mo^{6+} generation was confirmed by the recycled Py_4 sample XPS spectra. As mentioned earlier, Mo-doping ensures better charge separation than otherwise.[35]

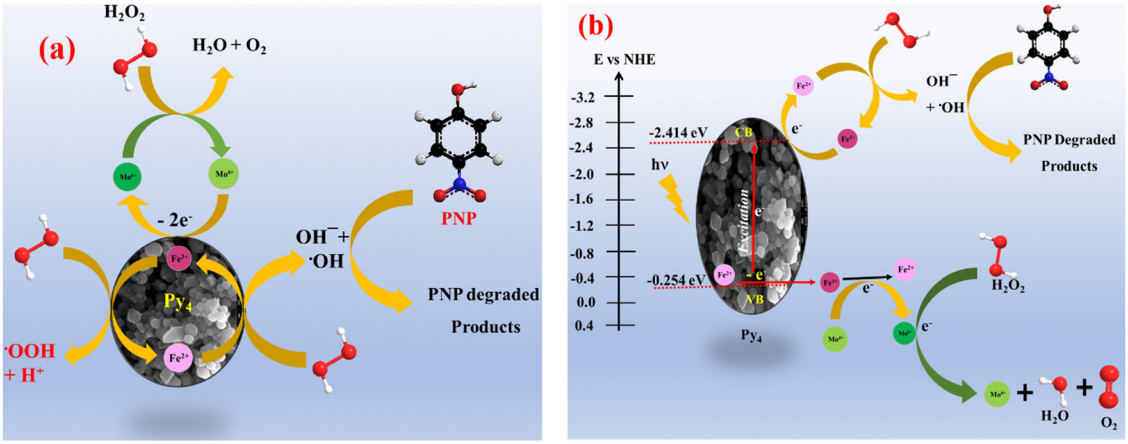

Fig. 7 Proposed (a) Fenton and (b) photo-Fenton mechanism of PNP degradation in the Mo-doped FeS_2.

4 Conclusions

In this work, undoped and Mo-doped iron pyrite materials were synthesized using a solvothermal method. XRD and DFT investigations showed that the dopant Mo substituted Fe in the FeS_2 lattice. Furthermore, XPS and DFT density of states analysis indicated Mo contribution to the VB of the doped FeS_2. PL spectra showed the slowest recombination kinetics for the Py_4 sample. Among the prepared FeS_2 samples, Py_4 (4 mol% Mo-doped) demonstrated the best (dark) Fenton and photo-Fenton catalytic activity for PNP degradation. Furthermore, photo-Fenton PNP TOF degradation values of all samples were substantially better than their Fenton TOF values. Another vital aspect was the significantly better recyclability of the catalysts under visible light photo-Fenton conditions. It appears that the Mo^{4+} dopant enhances the reusability of the catalyst by reducing the Fe^{3+} produced to Fe^{2+} during the Fenton and photo-Fenton process while itself getting regenerated by H_2O_2 oxidation. Since Mo^{4+} itself does not reduce H_2O_2, its substitution of Fe in FeS_2 would reduce the forward H_2O_2 reduction activity of the material. Besides this, only 8.33 mmol per liter and 1.66 mmol per liter. H_2O_2 was required for optimum Fenton and photo-Fenton PNP degradation. These H_2O_2 levels are appreciably lower than other recent reports. Catalyst Py_4 appears to have the best H_2O_2 normalized TOF value for photo-Fenton PNP degradation.

Data availability

The data supporting this article have been included as part of the ESI.†

Conflicts of interest

There are no conflicts to declare.

Acknowledgements

Maheswari Yadav acknowledges the financial support (JRF) received from IIT (BHU). The authors are also thankful to CCIS IIT (BHU) for computational facilities. We also acknowledge the Department of Chemistry for using the PL facility there. The authors thank CIF, IIT(BHU) for materials characterization facilities.

References

1 M. Pera-Titus, V. García-Molina, M. A. Baños, J. Giménez and S. Esplugas, Degradation of chlorophenols by means of advanced oxidation processes: a general review, *Appl. Catal., B*, 2004, **47**(4), 219–256.
2 H. Ren, X. Jin, C. Li, T. Li, Y. Liu and R. Zhou, Rosmarinic acid enhanced Fe(III)-mediated Fenton oxidation removal of organic pollutants at near neutral pH, *Sci. Total Environ.*, 2020, **736**, 139528.
3 J. Xiao, C. Wang, S. Lyu, H. Liu, C. Jiang and Y. Lei, Enhancement of Fenton degradation by catechol in a wide initial pH range, *Sep. Purif. Technol.*, 2016, **169**, 202–209.
4 Y. Lee and W. Lee, Degradation of trichloroethylene by Fe(II) chelated with cross-linked chitosan in a modified Fenton reaction, *J. Hazard. Mater.*, 2010, **178**(1–3), 187–193.
5 S. A. Messele, C. Bengoa, F. E. Stüber, J. Giralt, A. Fortuny, A. Fabregat and J. Font, Enhanced degradation of phenol by a Fenton-like system (Fe/EDTA/H_2O_2) at circumneutral pH, *Catal.*, 2019, **9**(5), 474.
6 R. Zhou, N. Shen, J. Zhao, Y. Su and H. Ren, Glutathione-coated Fe_3O_4 nanoparticles with enhanced Fenton-like activity at neutral pH for degrading 2,4-dichlorophenol, *J. Mater. Chem. A*, 2018, **6**(3), 1275–1283.
7 X. Da, D. Tang, L. Wang and J. Ma, Glutathione promoted Fenton degradation: a cocatalyst based on the -HS/-S-S- cycle with hydroxyl radicals, *Environ. Sci.: Water Res. Technol.*, 2020, **6**(3), 515–522.
8 S. Bae, D. Kim and W. Lee, Degradation of diclofenac by pyrite catalyzed Fenton oxidation, *Appl. Catal., B*, 2013, **134**, 93–102.
9 T. Liu, N. Chen, Y. Deng, F. Chen and C. Feng, Degradation of *p*-nitrophenol by nano-pyrite catalyzed Fenton reaction

with enhanced peroxide utilization, *RSC Adv.*, 2020, **10**(27), 15901–15912.
10 C. Liu, H. Yi, B. Yang, F. Jia and S. Song, Activation of Fenton reaction by controllable oxygen incorporation in MoS_2–Fe under visible light irradiation, *Appl. Surf. Sci.*, 2021, **566**, 150674.
11 D. Huang and J. Zhao, Speeding up Fenton reactions with a heterogeneous inorganic co-catalyst, *Chem.*, 2020, **6**(7), 1512–1514.
12 S. Venkateshalu, P. G. Kumar, P. Kollu, S. K. Jeong and A. N. Grace, Solvothermal synthesis and electrochemical properties of phase pure FeS_2 for supercapacitor applications, *Electrochim. Acta*, 2018, **290**, 378–389.
13 D. Wang, Q. Wang and T. Wang, Shape controlled growth of pyrite FeS_2 crystallites via a polymer-assisted hydrothermal route, *CrystEngComm*, 2010, **12**(11), 3797–3805.
14 J. P. Perdew, K. Burke and M. Ernzerhof, generalized gradient approximation made simple, *Phys. Rev. Lett.*, 1996, **77**(18), 3865.
15 A. K. De, N. Kamal, U. Kumar, N. Jatav and I. Sinha, The bandgap of sulfur-doped Ag_2O nanoparticles, *Phys. Chem. Chem. Phys.*, 2022, **25**(3), 2320–2330.
16 H. B. Wang, J. Q. Wang, R. Zhang, C. Q. Cheng, K. W. Qiu, Y. J. Yang, J. Mao, H. Liu, M. Du, C. K. Dong and X. W. Du, Bionic design of a Mo(IV)-doped FeS_2 catalyst for electroreduction of dinitrogen to ammonia, *ACS Catal.*, 2020, **10**(9), 4914–4921.
17 L. H. Ahrens, The use of ionization potentials Part 1. Ionic Radii of the elements, *Geochim. Cosmochim. Acta*, 1952, **2**(3), 155–169.
18 R. D. Shannon, Revised effective ionic radii and systematic studies of interatomic distances in halides and chalcogenides, *Acta Crystallogr., Sect. A: Cryst. Phys., Diffr., Theor. Gen. Crystallogr.*, 1976, **32**(5), 751–767.
19 A. Dolgonos, T. O. Mason and K. R. Poeppelmeier, Direct Optical band gap measurement in polycrystalline semiconductors: a critical look at the Tauc Method, *J. Solid State Chem.*, 2016, **240**, 43–48.
20 Z. López-Cabaña, C. M. S. Torres and G. González, Semiconducting properties of layered cadmium sulphide-based hybrid nanocomposites, *Nanoscale Res. Lett.*, 2011, **6**, 1–8.
21 S. Middya, A. Layek, A. Dey and P. P. Ray, Synthesis of nanocrystalline FeS_2 with increased band gap for solar energy harvesting, *J. Mater. Sci. Technol.*, 2014, **30**(8), 770–775.
22 H. Sun and P. Tang, Visible-light driven FeS_2 nanosized photocatalysts prepared by solvothermal method, *Adv. Mater. Res.*, 2012, **486**, 55–59.
23 Y. Ahmed, J. Zhong, W. Wang, L. Wang, Z. Yuan and J. Guo, Simultaneous removal of antibiotic-resistant bacteria, antibiotic resistance genes, and micropollutants by FeS_2@GO-based heterogeneous photo-Fenton process, *Environ. Sci. Technol.*, 2022, **56**(21), 15156–15166.
24 H. Liu, F. Liu, J. Zhang, J. Zhou, W. Bi, J. Qin, Q. Hou, Y. Ni, S. Xu and C. Yang, Degradation of methyl orange by pyrite activated persulfate oxidation: mechanism, pathway, and influences of water substrates, *Water Sci. Technol.*, 2022, **85**(10), 2912–2927.
25 Y. Cai, Y. Pan, J. Xue, Q. Sun, G. Su and X. Li, Comparative XPS study between experimentally and naturally weathered pyrites, *Appl. Surf. Sci.*, 2009, **255**(21), 8750–8760.
26 H. W. Wang, P. Skeldon and G. E. Thompson, XPS Studies of MoS_2 formation from ammonium tetrathiomolybdate solutions, *Surf. Coat. Technol.*, 1997, **91**(3), 200–207.
27 F. Pei, S. Wu, G. Wang, M. Xu, S. Y. Wang, L. Y. Chen and Y. Jia, Electronic and optical properties of noble metal oxides M_2O (M = Cu, Ag, and Au): first-principles study, *J. Korean Phys. Soc.*, 2009, **55**(3), 1243–1249.
28 D. Banjara, Y. Malozovsky, L. S. Franklin and D. Bagayoko, First-principles studies of electronic, transport and bulk properties of pyrite FeS_2, *AIP Adv.*, 2018, **8**(2), 025212.
29 J. Cai and M. R. Philpott, Electronic structure of bulk and (001) surface layers of pyrite FeS_2, *Comput. Mater. Sci.*, 2004, **30**, 358–363.
30 J. Xie, S. Wu, C. Luo, J. Zou, Y. Lin, S. He and C. Yang, Modulating Electronic Structure of Active Sites on Iron-Based Nanoparticles Enhances Peroxymonosulfate Activation, *Appl. Catal., B*, 2024, **354**, 124138.
31 J. Zou, S. Wu, Y. Lin, S. He, Q. Niu, X. Li and C. Yang, Electronic Phosphide-Support Interactions in Carbon-Supported Molybdenum Phosphide Catalysts Derived from Metal-Organic Frameworks, *Nano Lett.*, 2023, **23**(23), 10955–10963.
32 A. K. Hassan, M. A. Atiya and Z. A. Mahmoud, Photo-Fenton-like Degradation of Direct Blue 15 Using Fixed Bed Reactor Containing Bimetallic Nanoparticles: Effects and Box–Behnken Optimization, *Environ. Technol. Innovation*, 2022, **28**, 102907.
33 M. Nekoeinia, S. Yousefinejad, F. Hasanpour and M. Yousefian-Dezaki, Highly Efficient Catalytic Degradation of P-Nitrophenol by Mn_3O_4·CuO Nanocomposite as a Heterogeneous Fenton-like Catalyst, *J. Exp. Nanosci.*, 2020, **15**(1), 322–336.
34 T. Tang, B. Jin and P. Zhao, Preparation of the photo-Fenton agent MIL-100 (Fe) with high performance in the degradation of nitro explosives, *New J. Chem.*, 2023, **47**(18), 8566–8577.
35 B. Zhao, G. Mele, I. Pio, J. Li, L. Palmisano and G. Vasapollo, Degradation of 4-Nitrophenol (4-NP) Using Fe–TiO_2 as a Heterogeneous Photo-Fenton Catalyst, *J. Hazard. Mater.*, 2010, **176**(1–3), 569–574.
36 M. A. McKibben and H. L. Barnes, Oxidation of Pyrite in Low Temperature Acidic Solutions: Rate Laws and Surface Textures, *Geochim. Cosmochim. Acta*, 1986, **50**(7), 1509–1520.
37 J. De Laat and H. Gallard, Catalytic decomposition of hydrogen peroxide by Fe(III) in homogeneous aqueous solution: mechanism and kinetic modeling, *Environ. Sci. Technol.*, 1999, **33**(16), 2726–2732.
38 Y. Yang, Q. Wang, R. Aleisa, T. Zhao, S. Ma, G. Zhang, T. Yao and Y. Yin, MoS_2/FeS nanocomposite catalyst for efficient Fenton reaction, *ACS Appl. Mater. Interfaces*, 2021, **13**(44), 51829–51838.

39 M. Xing, W. Xu, C. Dong, Y. Bai, J. Zeng, Y. Zhou, J. Zhang and Y. Yin, Metal sulfides as excellent co-catalysts for H_2O_2 decomposition in advanced oxidation processes, *Chem.*, 2018, **4**(6), 1359–1372.

40 L. Zeng, J. Gong, J. Dan, S. Li, J. Zhang, W. Pu and C. Yang, Novel visible light enhanced pyrite-Fenton system toward ultrarapid oxidation of *p*-nitrophenol: catalytic activity, characterization, and mechanism, *Chemosphere*, 2019, **228**, 232–240.